Applied Catalysis A: General 485 (2014) 123–132

Contents lists available at ScienceDirect

Applied Catalysis A: General

journal homepage: www.elsevier.com/locate/apcata

Ce-Pr mixed oxides as active supports for Water-gas Shift reaction: Experimental and density functional theory characterization

Eduardo Poggio-Fraccari, Beatriz Irigoyen, Graciela Baronetti, Fernando Mariño*

ITHES, UBA-CONICET, Pabellón de Industrias, Ciudad Universitaria, (1428) Ciudad Autónoma de Buenos Aires, Argentina

ARTICLE INFO

Article history:
Received 9 June 2014
Received in revised form 25 July 2014
Accepted 28 July 2014
Available online 6 August 2014

Keywords:
Ce-Pr mixed oxides
DFT calculations
Oxygen storage capacity
Water-gas Shift reaction

ABSTRACT

Experimental measurements by several techniques and density functional theory (DFT) calculations are combined to characterize Ce-Pr mixed oxides and deeply understand the influence of Pr dopant in their geometric and electronic structure, reducibility and catalytic behavior concerning the Water-gas Shift reaction (WGSR). Samples with nominal Pr dopant content of 0, 5, 15 and 50 at% (atomic percentage) are synthesized via urea decomposition method and subsequent calcination in air at 450 °C. X-ray diffraction characterization shows an increase of ceria lattice parameter for Pr loadings lower than 15 at%, which is consistent with a solid solution formation. X-ray photoelectron spectra indicate a surface enrichment in Pr cations and a diminution of Ce^{3+} surface concentration as Pr content increases. DFT calculations confirm the preferential reduction of Pr cations due to a single oxygen vacancy formation in Ce-Pr mixed oxides, and also a significant decrease in the energy needed for this O removal compare to that in pure CeO_2. Both experimental measurements and DFT calculations evidence that the addition of Pr dopant to ceria promotes oxygen vacancies formation, redox properties and oxygen storage capacity (OSC). Even more, the same promoting effect of Pr in the WGSR intrinsic catalytic activity of Ce-Pr mixed oxides is observed.

1. Introduction

CeO_2 (ceria) is one of the most used rare earth oxides, related to a potential redox chemistry involving Ce^{3+} and Ce^{4+} ions. There are several areas of application of ceria, such as polishing agent in glasses [1,2] its uses in phosphors [3] and, mainly, its use in catalysis, due to above mentioned redox properties. CeO_2 is extensively used in three way catalysts (TWC) in vehicle engines, to reduce NO_x and simultaneously oxidize CO and not converted hydrocarbons [4]. The key function of ceria in these catalysts is associated to its great oxygen storage capacity (OSC), which allows the catalytic operation under oxidizing and reducing atmospheres [5,6]. In order to achieve better thermal stability and OSC, the addition of Zr to ceria was studied [7]. Other cations were also tested: some authors stated that OSC could be improved by doping ceria with La [8,9] or Pr [10]. The effects of Pr dopant on the redox thermodynamics of bulk CeO_2 were also investigated using first-principles density functional theory (DFT) calculations [11], and a combined theoretical DFT and experimental approach [12]. For a CeO_2 bulk supercell with a Pr dopant concentration of 3.125 at%, it was reported a decreasing in the oxygen vacancy formation energy, compared with that in pure ceria model, mainly originated from electronic and structural modifications [11,12]. As well, Ce-Pr mixed oxides were tested as supports for catalysts in several redox reactions such as the combustion of soot, CH_4 or CO [13–15]. However, in the case of catalysts for the Water-gas Shift reaction (WGSR), ceria was usually doped with trivalent rare earths like La, Sm o Nd [16]. Recently, WGSR has again attracted attention for non-traditional applications of hydrogen as combustible for fuel cells. In this respect, the Pt catalysts used in proton exchange membrane (PEM) fuel cells are poisoned if CO levels in the feed stream are higher than 20 ppm. Therefore, WGSR may be used to partially eliminate the CO in the upstream purification stage. Since the WGSR is exothermic, thermodynamic equilibrium is favored at lower temperatures where this reaction is kinetically limited. Hence, it is important to find a support with better redox properties and oxygen storage capacity, to enhance the activity of WGSR catalysts even at low temperatures. In this concern, Lin et al. tested bimetallic Cu-Ni catalysts supported on ceria doped with La [17]. In a previous work, we have tested Ce-Pr mixed oxides as supports for WGSR catalysts and found better performance of samples with low Pr loadings [18]. Therefore, in the present work we employed several experimental characterization techniques together with DFT theoretical calculations to deeply

* Corresponding author.
E-mail addresses: fernando@di.fcen.uba.ar, fernandojmarinio@gmail.com (F. Mariño).

http://dx.doi.org/10.1016/j.apcata.2014.07.040
0926-860X/

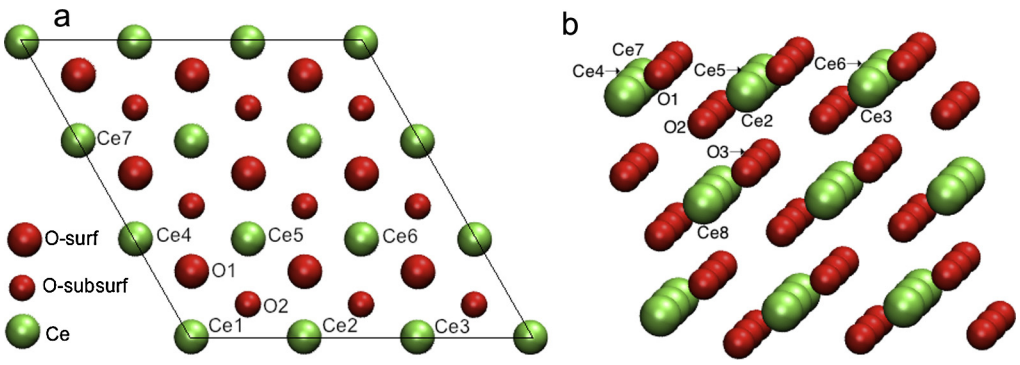

Fig. 1. The CeO_2(1 1 1) slab with p(3 × 3) expansion of the surface unit cell. (a) Top view. b) Lateral view.

understand the role of Pr in promoting the redox and OSC properties of Ce-Pr mixed oxides. Finally, we examined the relationship between their OSC and WGSR rate.

2. Experimental

Cerium-praseodymium mixed oxides, hereafter called CePrX, where X is the percentage atomic ratio (at%) between [Pr] and ([Pr] + [Ce]), and the corresponding precursors (called PCePrX) were studied throughout this work. Precursors were synthesized by the urea method [19,20], with different Pr contents (5, 15, and 50 at%). $Ce(NO_3)_3.6H_2O$ (Fluka >99.0%) and $Pr(NO_3)_3.6H_2O$ (Aldrich 99.9%) were dissolved and diluted separately in distillate water and then mixed together with an urea solution, keeping a total cation concentration of 0.1 M and a urea concentration of 1 M. Subsequently, this solution was aged in a thermostatic bath at 90 °C for 24 h. Finally, after centrifuging and washing three times, a pale green precursor was obtained (white solid in the case of pure cerium precursor). Calcination of samples was conducted from RT to 450 °C with a ramp of 10 °C/min, maintaining this final temperature during 5 h. Surface area and porosity values of the solids were obtained at 77 K over a wide range of relative pressures from 0.05 to 0.995, using an ASAP 2020 apparatus. UV–vis diffuse reflectance spectrum has been recorded with a Shimadzu UV-2600 spectrophotometer. XRD patterns were collected using the graphite-filtered Cu K_α radiation (λ = 1.5406 Å) in a Siemens D5000 powder diffractometer. Raman spectra were recorded using a LabRam spectrometer (Horiba-Jobin-Yvon) coupled to an Olympus confocal microscope (a 100× objective lens was used for simultaneous illumination and collection), equipped with a CCD detector cooled to about 200 K using Peltier effect. The excitation wavelength was in all cases 532 nm (Spectra Physics argon-ion laser). The laser power was set at 30 mW. XPS measurements were carried out with a multitechnical system (SPECS) equipped with a dual X-ray source of Mg/Al and a hemispheric synthesizer PHOIBOS 150. Spectra were acquired with a step energy of 30 eV using Al-K_α radiation operated at 200 W and 12 kV. The pressure of the chamber was lower than 10^{-9} mbar. The analyzed regions were Ce 3d, and Pr 3d. To remove the surface charging effects, the binding energies were calibrated using the Ce^{4+} (u''') signal at a 916.7 eV as a reference [21]. Background subtraction (Shirley) and peak fitting were performed using a commercial software CasaXPS® v2.3.15. SEM micrographs were acquired with a Zeiss microscope Zupra 40 model, equipped with Gemini Column and field electron emission. Catalytic activity in WGSR was evaluated in a fixed bed reactor using 240 mg of solid, diluted with a ceramic inert. The total inlet flow was equal to 85 cm^3/min, with a CO flow of 6 ml/min and a H_2O/CO ratio equal to 3/1 (with N_2 as balance). Previous to catalytic test, the solid was cleaned at 400 °C with air flow during 30 min, purged with N_2, reduced with 150 cm^3/min of H_2 (50% in N_2) and purged again with N_2. Finally, the temperature was raised to 450 °C under the reactant flow. The analysis of CO converted and the concentration of other gaseous products were performed in a Hewlett Packard gas chromatograph equipped with a Thermal Conductivity Detector (TCD).

3. Computational methods

First-principles density functional theory (DFT) calculations were carried out with the Vienna Ab-initio Simulation Package (VASP) [22,23]. We performed spin polarized calculations representing core electrons with the projector augmented wave (PAW) method [24], solving Kohn–Sham equations with the generalized gradient approximation (GGA) and using the exchange-correlation functional of Perdew–Burke–Ernzerhof (PBE) [25]. The cutoff energy of the plane wave basis was set to 480 eV, while using the valence configurations $5s^2$, $5p^6$, $6s^2$, $5d^1$, $4f^1$ for Ce; $5s^2$, $5p^6$, $6s^2$, $5d^1$, $4f^2$ for Pr; and $2s^2$, $2p^4$ for O. The Brillouin zones were sampled with the Monkhorst–Pack scheme [26]. Structural relaxations were performed according to the Hellmann–Feynman approximation and the atomic positions were relaxed until the force acting on each atom was smaller than 0.02 eV/Å.

The standard DFT formulation usually fails to describe strongly correlated electrons due to a deficient treatment of electron correlation. This limitation has been corrected to some extent by using the DFT + U method, where the introduction of a Hubbard parameter U modified the electron self-interaction error and enhanced the description of the correlation effects [27,28]. Accordingly, we used the Hubbard parameters: U_{eff} = 5 eV for Ce(4f) states, and U_{eff} = 4.5 eV for Pr(4f) orbitals. The U_{eff} value of 5 eV was chosen for the Ce(4f) states as it correctly described the atomic and electronic structure of both CeO_2 and CeO_{2-x} systems [29–31]. On the other hand, the value of U_{eff} = 4.5 eV has shown to reproduce the experimentally available data for PrO_2, such as lattice constant and band gap, and was reliable for the description of the strong on-site Coulomb repulsion among Pr(3d) electrons [11].

Previously reported DFT works have studied oxygen defects formation into the bulk crystal lattice of Ce-Pr mixed oxides, modeling a $Ce_{0.96875}Pr_{0.03125}O_2$ system with a 2 × 2 × 2 supercell [11,12]. Both works used the PBE method and the Hubbard correction for Ce(4f) electrons, considering an effective U value of 4.5 eV [11], and 5.3 eV [12]. In adittion, as mentioned before, a Hubbard parameter U_{eff} = 4.5 eV was used for Pr(4f) orbitals in Ref. [11].

In the present work, two different Pr-doped CeO_2(1 1 1) slabs, with low (3.7 at%) and high (25 at%) amount of Pr dopant, were employed for achieving a detailed description of Pr effect in the surface chemistry of Ce-Pr mixed oxides. The catalytic surface was represented with the (1 1 1) plane because it is the most stable among the low-index (1 1 1), (1 1 0), and (1 0 0) surfaces of ceria and it corresponds to minimal Ce-O bonds cleavage [32–35].

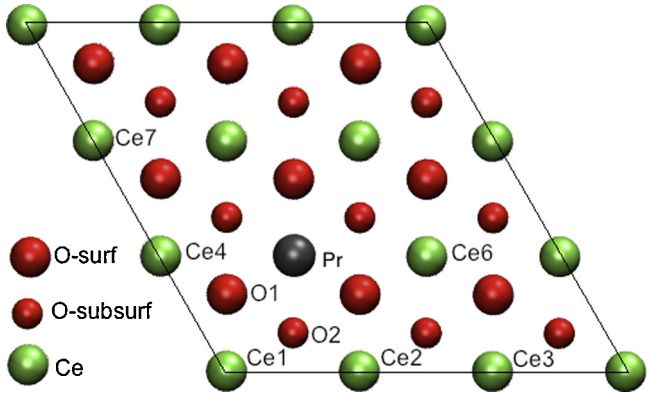

Fig. 2. The $Ce_{0.963}Pr_{0.037}O_2$(1 1 1) surface with p(3 × 3) expansion of the surface unit cell.

Both low-doped (3.7% Pr) and undoped CeO_2 (1 1 1) surfaces were modeled by a $p(3 \times 3)$ slab. The first step of our calculations involved bulk CeO_2 structure optimization with respect to lattice constant. From this, a value of $a = 5.49$ Å was obtained. Then, the CeO_2(1 1 1) surface was built by cleaving the optimized bulk cell with the (1 1 1) plane and retaining an extra oxygen layer (see Fig. 1).

The Pr-doped CeO_2(1 1 1) surface with low content of Pr was constructed by substituting one surface Ce cation with a Pr dopant in the CeO_2(1 1 1) slab with p(3 × 3) expansion of the surface unit cell (see Fig. 2). This substitution gives a Pr concentration of 3.7 at% related to the total number of Pr and Ce cations.

The resulting $Ce_{0.963}Pr_{0.037}O_2$(1 1 1) slab has 9 atomic layers and an empty space of 18 Å, which was introduced to avoid periodic interactions with the atoms of the upper image. Besides, the Brillouin zone was sampled with a 3 × 3 × 1 k-points mesh.

On the other hand, the Pr-doped CeO_2(1 1 1) surface with high content of Pr was generated from an optimized 12-atom unit cell of ceria with 25% of Ce cations replaced by Pr (see Fig. 3a). The optimization of this bulk structure resulted in a lattice constant value of 5.49 Å, similar to that computed for the fluorite-type CeO_2 structure. The corresponding p(2 × 2) slab, hereafter named as $Ce_{0.75}Pr_{0.25}O_2$(1 1 1), has 12 atomic layers, a vacuum space of 18 Å, and contains one Pr atom (25 at%) in each of the cation layers (see Fig. 3b). In this case, the Brillouin zone was sampled with a 4 × 4 × 1 k-points grid.

Energy calculations for CeO_2(1 1 1), $Ce_{0.963}Pr_{0.037}O_2$(1 1 1) and $Ce_{0.75}Pr_{0.25}O_2$(1 1 1) slabs were performed allowing atomic coordinates of Ce, Pr and O ions located in the six uppermost layers to fully relax; while those of the ions placed in the bottom layers were fixed to their bulk positions. Meanwhile, the electronic effects of Pr doping in CeO_2-based systems were studied through the analysis of electron occupancy of Ce(4f) and Pr(4f) states, and the Bader charge of Ce and Pr cations [36].

4. Results and discussion

The mixed solids employed in this work, were obtained by the precipitation of Ce and Pr precursors by thermal decomposition of urea and subsequent calcination procedure. This method has proved to be adequate for the synthesis of Ce, Ce-Cu, Ni-Cu, and Zn-Cu samples [19,20,37,38]. The evolution of pH during the precipitation of precursors was followed by extracting aliquots of supernatant solution (Supplementary Information Figure S1).

As it can be seen, the evolution of pH is similar for all samples, with a starting value of approximately 5 and an ending one close to 8. The same values were found for a precursor of pure ceria that we have studied in a previous work [19]. Therefore, Ce-Pr mixed precursors present similar behavior than pure Ce or Pr ones, with Ce and Pr precipitating together and almost all cations (more than 99%) being present in the solid phase after 8 h of reaction [18].

The reflections found in the XRD patterns of the precursors (see Supplementary Information Figure S2), were due to basic carbonates with orthorhombic structure and also to the stable form of these rare earths (Ce and Pr) compounds with hexagonal structure [39]. It is known that the signals of orthorhombic JCPDS No. 41-0013 (for Ce) and JCPDS N° 26-1349 (for Pr), are undistinguishable. The same fact occurs with hexagonal structure, JCPDS No. 52-0352 and JCPDS No. 27-1376, for $Ce(OH)CO_3$ and $Pr(OH)CO_3$ respectively; some characteristic reflections are shown in Figure S2.

The decomposition processes of the precursors under oxygen atmosphere (see Supplementary Information Figure S3), are essentially similar for samples with Pr content lower than 15 at%. They present a single step centered at a temperature close to 260 °C, as it was observed for the decomposition of a pure ceria precursor in the same conditions [19]. These results might imply that mixed basic carbonates are obtained, where Pr replaces Ce ions in the lattice as it was observed for La-doped ceria [40] or Ce-Pr mixed oxides [41] synthesized in similar conditions. On the other hand, the thermogravimetric profile of a high Pr content sample (CePr50) is similar to those of the precursors with low amount of Pr (CePr5 and CePr15), but the signal becomes flat at a significantly higher temperature, close to 500 °C. This result indicates a promoting effect of Ce in the decomposition process of CePrX samples as it can be concluded comparing our results with those of pure praseodymium thermal decomposition profile reported by Zhang et al. [42].

Calcined samples were dissolved in orthophosphoric acid and then analyzed by ICP-MS. The results indicate that the expected Pr content is similar to that obtained by chemical analysis for small Pr loadings, but they deviate practically 20% for the sample with the highest Pr content [18]. These results suggest a limitation of the Pr amount that could be incorporated using these synthesis conditions. In fact, other authors also found limitations to incorporate more than 30 at% of Pr into the ceria lattice [43,44].

XRD patterns of Ce-Pr mixed oxides presented in a previous work only showed the characteristic reflections of CeO_2 (JCPDS No. 42-1002) and PrO_2 (JCPDS No. 65-0325) [18]. Since there was no evidence that other Pr oxides (such as Pr_2O_3 or Pr_6O_{11}) were present in the samples, it is feasible that a solid solution between cerium and praseodymium was formed, due to the similar ionic radius of Ce^{4+} and Pr^{4+} cations [13,45,46]. XRD patterns of the main reflection of Ce-Pr mixed oxides, corresponding to the (1 1 1) plane, show that this signal shifts to lower angles as Pr content increases. This result could be interpreted through a lattice parameter expansion, as reported in Table 1. Since the ionic radius of trivalent ions, Ce^{3+} (0.114 nm) or Pr^{3+} (0.113 nm), are larger than that of Ce^{4+} (0.097 nm) or Pr^{4+} (0.096 nm), it is possible that tetravalent ions are replaced by those in the reduced state. It is worth mention that both oxidation states of Ce were found by XPS measurements as it will be described later in this work. As it can be seen, the lattice parameter proportionally increases for small Pr loadings (<15 at%) which is consistent with a solid solution formation [47–49]. In the case of CePr50 sample, the lattice parameter does not follow the same trend, with a lattice parameter very similar to that of CePr15. This might occurs either by the segregation of two ceria phases, as it was found for a Ce-La system [47], or by the formation of a solid solution with high oxygen vacancies concentration, leading to a shrinkage of the lattice [50,51]. The latter assumption is in agreement with Raman results that would be presented later in this work. The crystallite size (estimated by Scherrer's equation) decreases as Pr content increases [18]. The smallest surface area found for CePr50 despite of the lowest crystallite size reported for the same sample might be explained by crystallite agglomeration. Tok et al. [43] explained this fact by analyzing different

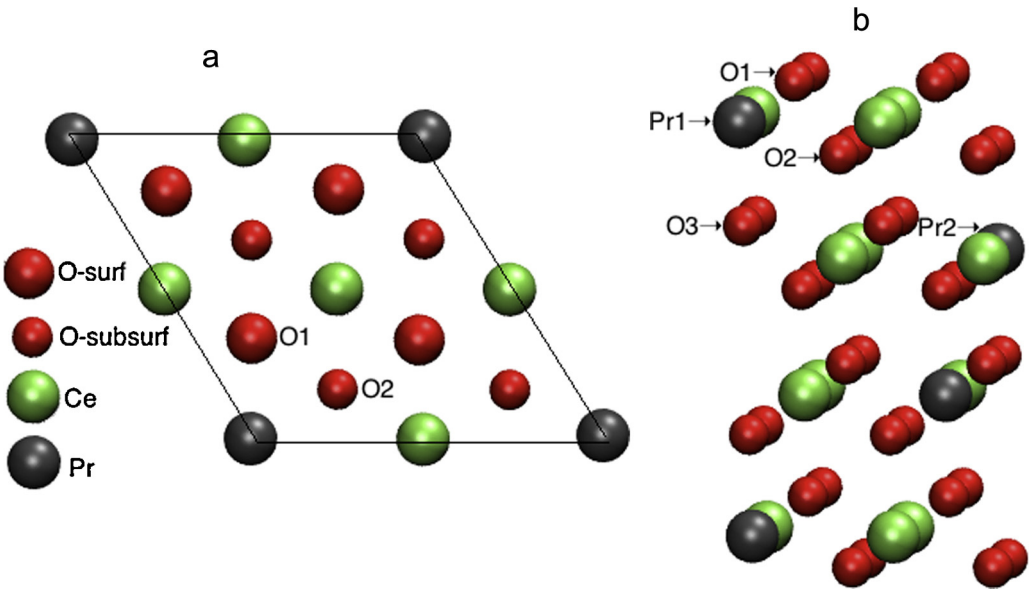

Fig. 3. The $Ce_{0.75}Pr_{0.25}O_2$(1 1 1) slab with p(2 × 2) expansion of the surface unit cell. (a) Top view. (b) Lateral view.

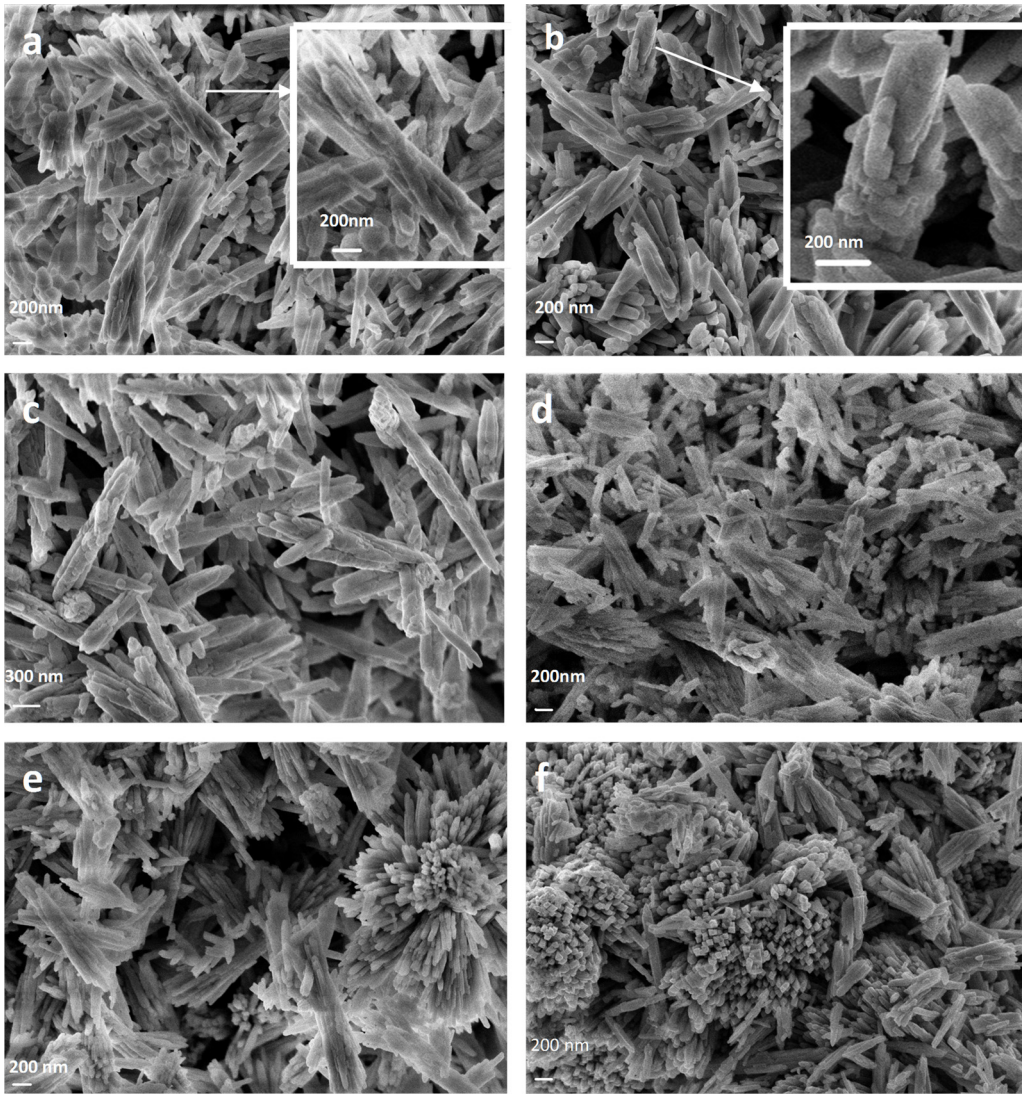

Fig. 4. SEM micrographs of Ce-Pr samples: (a) CePr0 precursor, (b) CePr15 precursor, (c) CePr0, (d) CePr5, (e) CePr15, (f) CePr50.

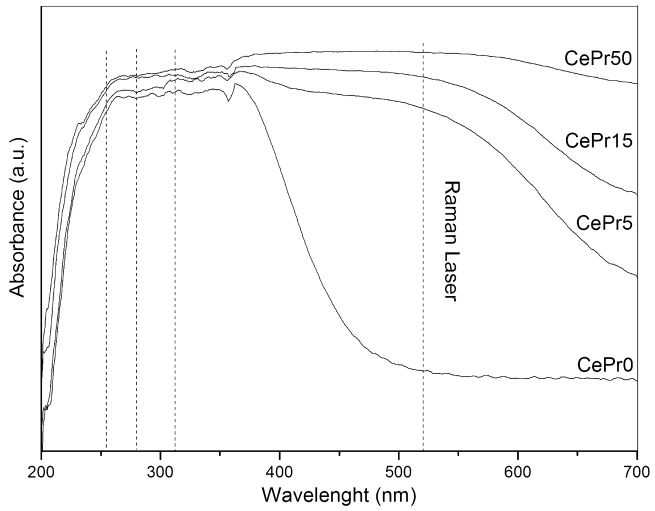

Fig. 5. UV–vis diffuse reflectance of Ce-Pr samples.

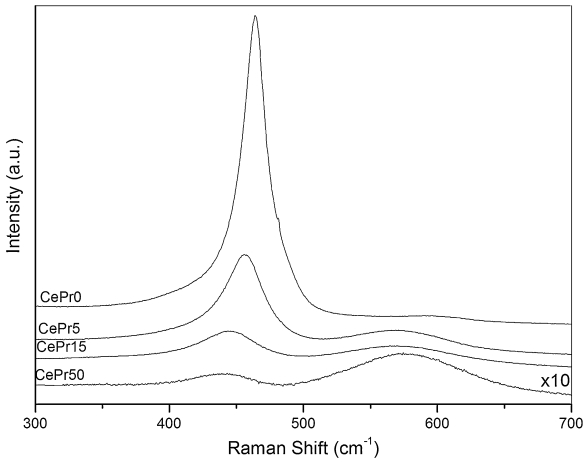

Fig. 6. Raman spectra of Ce-Pr samples.

pH or aging time needed to precipitate Ce doped solids. In their conditions, successive nucleation occurred hindering growth and resulting in crystallite agglomeration. In our previous work [18], we could roughly estimate the average number of crystallites in each particle from BET values, assuming spherical shapes. Comparing the values estimated by Scherrer (XRD) and BET area, crystallite agglomeration can be discarded in samples with low Pr content. Nevertheless, the agglomeration of crystals becomes evident for CePr50 sample since particle size estimation by BET was markedly higher than crystallite size determined by XRD [18]. SEM micrographs of samples are presented in Fig. 4. The solid precursors show rod-like particles (see Fig. 4a and b). The calcined samples retain a similar morphology (see Fig. 4c–f), as it was the case of pure ceria in one of our previous works [19].

According to the literature, the morphology of the samples influences the catalytic activity for CO oxidation [52], being the rod-shape particles the ones that preferentially expose the most reactive planes [53]. Particle shapes are strongly dependent on urea:cation ratio used during the precipitation procedure. In fact, Wang et al. [54] synthesized CeO_2 powders by hydrothermal method using urea as precipitating agent. In that work, an increase in the urea:cation ratio from 1:1 to 20:1 increased particle size and changed the morphology, from symmetric rhomboidal to prismatic shapes. In our case, with a 10:1 urea:cation ratio, a non-uniform particle distribution size is observed, with rods formed by smaller particles with ellipsoidal shape (see enlargement of Fig. 4a and b). In the case of Ce-Pr mixed oxides, some particles are agglomerated rods and form bundles.

The Ce-Pr samples are colored solids. CePr0 sample is a yellowish powder and the Ce-Pr mixed oxides change from orange to dark brown with the increase of Pr content in agreement with literature [41]. The UV–vis diffuse reflectance spectra obtained for these samples are shown in Fig. 5. CePr0 sample spectrum has a strong absorption band below 400 nm due to charge transfer transition from O^{2-} to Ce^{4+} close to 278 nm, interband transition at 313 nm [55], and charge transfer from O^{2-} to Ce^{3+} close to 255 nm [56]. Similar spectra were obtained for Ce-Pr samples below 400 nm.

However, at wavelengths higher than 400 nm, it must be noted that the replacement of Ce by Pr ions in the host lattice modifies the absorption of samples; this effect is evident even with a low content of Pr, such as 5 at%. In the case of these mixed oxides, a new band in the range 400–650 nm was also observed due to Pr ions transitions [57].

Furthermore, all samples were characterized by Raman spectroscopy and the results are shown in Fig. 6. The intensity of spectra decreases as Pr content increases, due to the stronger absorption of Ce-Pr mixed oxides at the wavelength used (514 nm), as it was seen by UV–vis (Fig. 5). According to Pu et al. [57], the information obtained is mainly representative of the surface when the excitation laser and the scattering light are strongly absorbed by the sample. The spectra show two bands: the main one close to 465 cm^{-1} and a secondary one at approximately 570 cm^{-1}. Fluorite structure only has a single Raman mode allowed, which has F_{2g} symmetry and can be viewed as a symmetric breathing mode of the O atoms around each cation [60]. In consequence, the main band is assigned to the fluorite structure of all samples. Upon the addition of Pr, a slight shift in the peak position to lower values is observed, without changes in the peak symmetry. These same features, observed by other authors in Ce, Ce-La or Ce-Pr samples, were assigned either to a change in the particle size inhomogeneous strains, lattice defects or oxygen vacancies [14,58–61]. The incorporation of an aliovalent cation as Pr in the fluorite lattice tends to form a nonstoichiometric oxide and induces lattice defects as oxygen vacancies. It is widely accepted in literature that the second band at 570 cm^{-1} is related to these defects [13,58,62]. To clarify this point, the ratio of the intensities of the bands at 570 and 465 cm^{-1}, called I_{570}/I_{465}, versus the Pr content of the samples is plotted in Fig. 7. This figure shows that both the value of I_{570}/I_{465} ratio and the shift of the main Raman band increase with the Pr content.

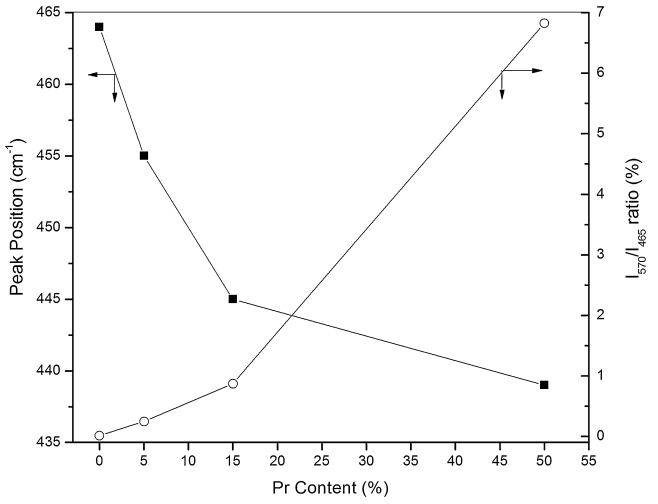

Fig. 7. Intensity ratio between signals at 570 and 480 cm^{-1} versus Pr content (left axis), Peak maximum position versus Pr content (right axis).

In a previous work [20], we have studied by XRD and XPS pure ceria samples calcined at several temperatures, in particular at 450 °C as it used in the present work. We had calculated the Ce^{3+} fraction by XRD, assuming the validity of Vergard's law, which states that there is a linear relation between a change in lattice parameter and molar fraction of dopants (in this case, Ce^{3+} is the dopant in Ce^{4+} lattice). The value found was much lower than Ce^{3+} fraction estimated by XPS, indicating that Ce^{3+} is mainly present on the surface of sample. The study of Ce 3d spectra was performed using nomenclature introduced by Burroughs [63], where Ce^{3+} presented two doublets (u_0, v_0, u', v') and Ce^{4+} three (u, v, u'', v'', u''', v'''). The u peaks and v peaks represent the $Ce3d_{2/3}$ and $Ce3d_{5/2}$ contributions respectively [64]. In order to obtain all the intensities, a deconvolution of Ce 3d spectra was performed [20], considering that: (i) the intensity ratio between peaks of doublet was close to 2/3; (ii) the peak position for all samples was allowing to vary 0.3 eV, and (iii) the FWHM for peaks of doublet was almost the same, with a difference less than 5%. With these conditions it was found that the doublet splitting is 18.4 eV as reported in literature [65]. As mentioned before, the Ce^{3+} fraction was estimated by the ratio between the peak intensities of this ion and those corresponding to Ce^{4+} y Ce^{3+} (see Supplementary Information Figure S4) [20,66–68].

With the objective of explaining the difference found in Ce^{3+} fraction using either XRD or a surface technique such as XPS, an additional study was made in this work over pure ceria (CePr0), modifying in each XPS experiment the angle measured from surface (take-off angle). Changing this parameter, it is possible to perform a depth profiling without using a destructive technique [69]. The measured intensity of an element is expressed in Equation (1), where K_A is a constant that involves the analyzed area, the X-ray flux, the instrument detection, and the sensitivity factor based on Scofield's photoionization cross sections; λ is the inelastic mean free path (IMFP); φ is the take-off angle; χ is the molar fraction at depth z [70,71].

$$I_A = K_A \int_0^\infty \chi_A e^{-z/\lambda \sin(\varphi)} dz \quad (1)$$

The simplest depth profile is a thin-uniform layer of Ce^{3+} over a substrate of Ce^{4+} ions in an infinite sample, i.e.: $z \gg 5\lambda$ [72]. By the integration of Equation 1 for an unknown "d" thickness of Ce^{3+} layer, two expressions for Ce ions can be obtained (see Equation (2)).

$$I_{Ce^{3+}} = K\chi_{Ce^{3+}} \left(1 - e^{-d/\lambda Ce^{3+} \sin(\varphi)}\right) \quad (2a)$$

$$I_{Ce^{4+}} = K\chi_{Ce^{4+}} e^{-d/\lambda Ce^{4+} \sin(\varphi)} \quad (2b)$$

From the ratio between intensities of both ions, K constant will be cancelled. Besides, the molar fraction of ions also will be cancelled because both Ce^{3+} and Ce^{4+} ions occupy the same positions in the fluorite lattice. The IMFP depends on the electron energy and composition. However, in our case these values are similar to each other, 1.23 and 1.09 nm for Ce^{3+} and Ce^{4+}, respectively [67]. So, other simplifying hypothesis can be made, by using an average value for IMFP [72]. With these assumptions and a linearization, Equation (3) is found, and it is used to fit the intensity ratio versus the take-off angle in Fig. 8.

$$\ln\left(\frac{I_{Ce^{3+}}}{I_{Ce^{4+}}} + 1\right) = \frac{d}{\lambda \sin(\varphi)} \quad (3)$$

Thus, the "d" parameter or the thickness of Ce^{3+} layer was obtained with a value equal to 0.11 ± 0.02 nm. This value is very similar to the atomic radius of Ce^{3+} (0.114 nm), indicating that Ce^{3+} is only present in the first atomic layer of the sample. This result is in agreement with those of other authors who have also found a core-shell distribution in pure ceria samples [49,73,74], with Ce^{4+} ions in the core and Ce^{3+} ions in the outer shell. These findings indicate that reduced Ce ions are stable on the ceria surface.

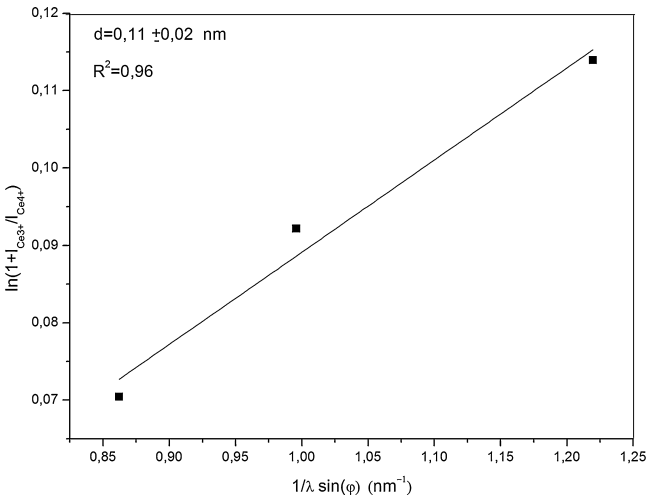

Fig. 8. Fitting of Ce^{3+}/Ce^{4+} intensities versus take off angle.

Table 1
BET, XRD and XPS results of samples.

Sample	BET AREA (m^2/g)	Lattice parameter (nm)	Ce^{3+} surface fraction (%)[a]	Pr/Ce surface content[b]
CePr0	110.1	0.542	6.7	–
CePr5	100.2	0.543	4.9	0.12
CePr15	89.4	0.544	3.1	0.28
CePr50	19.4	0.544	2.2	3.29

[a] Calculated as ratio between Ce^{3+} and Ce ions.
[b] Calculated as ratio between Pr and Ce ions.

On the other hand, the XPS measurements for Ce-Pr mixed oxides samples show that this Ce^{3+} surface fraction decreases with the increase of Pr content in the samples, as it can be observed in Table 1. Simultaneously, a surface enrichment of Pr occurs, suggesting that Pr ions tend to preferentially occupy surface positions and replace Ce^{3+} ions, as it can be seen in the last column of Table 1.

An important feature of catalysts for redox reactions is their oxygen storage capacity, OSC. A theoretical OSC value can be calculated by the estimation of the oxygen present at the surface of ceria samples, using the atomic density of low-index crystallographic planes and the surface area [75–77]. Obviously, this model predicts that OSC is proportional to the surface area exposed to the reduction by CO. For the samples studied in this work, the theoretical OSC values and the ratio between the experimental and theoretical OSC are reported in Table 2. This ratio is always lower than one and increases with the Pr content of the samples.

Table 2
OSC and WGSR results.

Sample	Theoretical OSC ($\mu mol_{CO}/g$)[a]	OSC_{exp}/OSC_{theo}[b]	Reaction rate per surface unit ($\mu mol/(s\,m^2)$)[c]
CePr0	624	0.08	1.43
CePr5	569	0.11	2.32
CePr15	506	0.10	2.43
CePr50	108	0.22	4.11

[a] Calculated using BET values.
[b] OSCexp Average among 5 pulses at 400 °C.
[c] Flow 85 ml/min, 8% CO, 24% H_2O, N_2 as balance, catalytic mass: 240 mg, CO conversion lower than 15% (differential reactor).

These results are in agreement with Raman spectra already presented, where the addition of Pr monotonically increases the intensity of the Raman peak at 570 cm^{-1}. That band is related to the generation of oxygen vacancies that enhances CO oxidation activity and/or OSC [14,75]. In our previous work [18], TPR profiles had also shown that the addition of Pr to ceria samples improved the reducibility of these solids. The experimental characterization has shown the addition of Pr improved oxygen removal and reducibility properties compared to pure ceria. However, the role of Pr dopant in the surface chemistry has still to be completely elucidated. In this concern, first-principles calculations are essential to provide a detailed understanding of the reactivity of ceria-based systems [78]. Thus, oxygen vacancies (surface and subsurface) formation and redox properties of Ce-Pr mixed oxides were evaluated by performing spin-polarized periodic DFT calculations.

Two Pr-doped CeO_2(1 1 1) slabs with 3.7 at% and 25 at% of Pr contents were considered for modeling stoichiometric Ce-Pr catalytic surfaces with low- and high-dopant concentration, respectively. The top view of CeO_2(1 1 1), $Ce_{0.963}Pr_{0.037}O_2$(1 1 1) and $Ce_{0.75}Pr_{0.25}O_2$(1 1 1) surfaces employed in our calculations are shown in Figs. 1a, 2a and 3a, respectively. The formation of these surfaces led to Pr-O and Ce-O bonds of similar length, in the interval between 2.31–2.42 Å. The average length of Pr-O bonds is equal to that of Ce-O bonds (2.38 Å). Concerning the electronic structure of stoichiometric Pr-doped CeO_2(1 1 1) slabs, we calculated an electron occupancy of Pr(4f) states of 1.35 electrons (see Table 3); which is consistent with that of 1.44 electrons reported for the bulk structure of $Ce_{0.9688}Pr_{0.0312}O_2$ and 1.5–1.6 electrons for that of PrO_2 [80–83]. We also computed the values of Bader charge for Ce and Pr cations in pure CeO_2(1 1 1) and Pr-doped CeO_2(1 1 1) systems (see Table 3). Accordingly, the corresponding oxidation states of Ce and Pr cations were estimated as Ce^{4+} and Pr^{4+}.

On the other hand, non-stoichiometric CeO_{2-x}(1 1 1) and Pr-doped CeO_{2-x}(1 1 1) systems were simulated by removing surface, subsurface and inner-layer oxygen atoms. These anions were labeled as O1, O2 and O3, respectively (see Figs. 1b, 3b). The surface oxygen O1 is a first-nearest neighbor to Pr dopant; while O2 and O3 are located in the second (subsurface) and third O-layer, respectively. These O-deficient systems, which cell parameters were fixed at the value of 5.49 Å (as calculated for pure CeO_2 bulk structure), were optimized with respect to Ce, Pr and O atomic positions.

The energy required to form an O-vacancy ($\Delta E_{O\text{-}Vac}$) was computed as:

$$\Delta E_{O\text{-}Vac} = E[CeO_{2-x}(1\,1\,1)] + 1/2E[O_2] - E[CeO_2(1\,1\,1)] \quad (4)$$

$$\Delta E_{O\text{-}Vac} = E[Ce_{0.963}Pr_{0.037}O_{2-x}(1\,1\,1)] + 1/2E[O_2] - E[Ce_{0.963}Pr_{0.037}O_2(1\,1\,1)] \quad (5)$$

$$\Delta E_{O\text{-}Vac} = E[Ce_{0.75}Pr_{0.25}O_{2-x}(1\,1\,1)] + 1/2E[O_2] - E[Ce_{0.75}Pr_{0.25}O_2(1\,1\,1)] \quad (6)$$

where $E[CeO_2(1\,1\,1)]$, $E[Ce_{0.963}Pr_{0.037}O_2(1\,1\,1)]$, and $E[Ce_{0.75}Pr_{0.25}O_2(1\,1\,1)]$ correspond to the energy of the relaxed stoichiometric CeO_2(1 1 1) and Pr-doped CeO_2(1 1 1) slabs; $E[CeO_{2-x}(1\,1\,1)]$, $E[Ce_{0.963}Pr_{0.037}O_{2-x}(1\,1\,1)]$, and $E[Ce_{0.75}Pr_{0.25}O_{2-x}(1\,1\,1)]$ indicate the energy of those slabs after introducing an O-defect; while, $E[O_2]$ is the energy of the oxygen molecule in vacuum. Note that, in the three cases (Equations (4–6)), a positive value of $\Delta E_{O\text{-}Vac}$ would indicate that energy is needed to form the O-vacancy.

The energy required for the formation of the surface O1 vacancy on pure ceria was calculated in 1.71 eV (see Table 3). This value is in agreement with that of 1.76 eV previously reported for surface O-defect formation on CeO_2(1 1 1) slab with p(4 × 4) expansion of the surface unit cell [78]. However, the creation of the O1-defect on both 3.7 at% and 25 at% Pr-doped ceria systems required only 1.00 eV as reported for single oxygen vacancy formation in $Ce_{0.9688}Pr_{0.0312}O_2$ bulk structure [11].

The comparison of our computed energy values for O-defect formation shows that the energy required for O2 removal is 0.16 eV lower than that for surface O1 removal. Previous PBE + U (U_{eff} = 4.5 eV) calculations in CeO_2(1 1 1) slab predicted the surface defect to be slightly more stable (0.08 eV) relative to the subsurface defect formation, while hybrid functional computations showed the subsurface O-defect to be more stable by 0.18 eV [78]. The results reported in Table 3, also show that formation of subsurface O2-defect was favored by Pr dopant; which decreased the required energy from 1.54 eV in pure CeO_2(1 1 1) to 1.02 eV and 0.5 eV in 3.7% and 25% Pr-doped CeO_2(1 1 1) systems, respectively.

Concerning the $Ce_{0.75}Pr_{0.25}O_2$(1 1 1) slab we note that O2 removal could be favored not only by Pr1 dopant, as seen for the $Ce_{0.963}Pr_{0.037}O_{2-x}$(1 1 1) system, but also by the Pr2 cation located in the fifth layer of the slab (see Fig. 3b). Similar behavior was detected for inner-layer O3-defect creation. In that sense, the calculations indicated that Pr significantly reduces the energy needed for oxygen vacancies formation. This theoretical indication is in agreement with our Raman results previously discussed. Besides, an increase in O-vacancies concentration for Pr-doped CeO_2 materials was also reported by other authors [57,83,84].

Cerium cations charge (from Bader analysis) and electron occupancy of Ce(4f) states in the reduced CeO_{2-x}(1 1 1) slab, which resulted from surface O1-defect formation, are reported in Table 3. The electron occupancy of Ce2(4f) and Ce3(4f) states was calculated in 0.97 electrons, while the Bader charge of Ce2 and Ce3 cations resulted in 9.85 and 9.86 electrons, respectively. Therefore, it can be concluded that removal of surface oxygen O1 from the CeO_2(1 1 1) slab led to reduction of two Ce^{4+} cations (Ce3 and Ce4) to Ce^{3+}, in order to keep the charge neutrality of the system. For pure CeO_2, it was reported that low-lying-empty Ce(4f) states can accommodate the two electrons left behind when an oxygen atom leaves the material [78]. In general, PBE + U calculations predict that an oxygen vacancy formation in the undoped CeO_2(1 1 1) system led to a stable reduced structure with the two electrons localized at Ce cations in the 1NN-1NN (first-nearest-neighbor), 2NN-2NN (second-nearest-neighbor) and 1NN-2NN positions related to that of the O-defect [78,85]. Note that our calculations predicted the reduction of Ce3 and Ce4 cations, which are the second-nearest neighbors of the O1-vacancy (see Fig. 1a).

On the other hand, the charge of Ce and Pr cations as well as the electron occupancy of (4f) states was analyzed for O-deficient Pr-doped CeO_{2-x}(1 1 1) slabs (see Table 3). Due to O1 removal from the $Ce_{0.963}Pr_{0.037}O_2$(1 1 1) system, the electron occupancy of Ce3(4f) and Pr(4f) states increased up to 0.96 and 1.97 electrons, respectively. The computed value for Pr(4f) orbitals (1.97 electron) is consistent with that of 1.96 electrons reported for Pr^{3+} in the $Ce_{0.9688}Pr_{0.0312}O_{1.9688}$ bulk structure [79]. Therefore, it can be concluded that surface O1-defect formation led to reduction of the Pr^{4+} dopant to Pr^{3+} as well as that of the Ce3 cation (see the position of Pr and Ce3 cations in Fig. 2). However, the removal of O1 from the $Ce_{0.75}Pr_{0.25}O_2$(1 1 1) slab resulted in electron localization at two Pr cations (see Table 3). Noticeably, Pr1 and also Pr2 were reduced despite the fact there are Ce cations which would have been reduced at 1NN and 2NN positions related to that of the O1 vacancy (see Fig. 3b).

Considering the formation of single O2- and O3-vacancy in pure CeO_2(1 1 1) slab, it can be seen this O removal led to the reduction of

Table 3
CeO_2(1 1 1) and Pr-doped CeO_2(1 1 1) systems. Calculated energy for a single O-vacancy formation ($\Delta E_{O\text{-}Vac}$), charge of Ce and Pr cations (Bader analysis) and electron occupancy of Ce(4f) and Pr(4f) states.

Undoped and Pr-doped CeO_2 (1 1 1) slabs		$\Delta E_{O\text{-}Vac}$, eV		Electron occupancy of the cations (4f) states, e			Bader charge, e	Estimated oxidation state
Stoichiometric slabs	CeO_2(1 1 1)				Ce	0	9.60	4+
					Ce2	0	9.60	4+
					Ce3	0	9.60	4+
	$Ce_{0.963}Pr_{0.037}O_2$(1 1 1)				Ce	0	9.60	4+
					Ce4	0	9.60	4+
					Pr	1.35	10.70	4+
	$Ce_{0.75}Pr_{0.25}O_2$(1 1 1)				Ce	0	9.64	4+
					Pr1	1.29	10.73	4+
					Pr2	1.18	10.70	4+
	CeO_{2-x}(1 1 1) with a surface O1-, O2- or O3-vacancy	O1	1.71	Surface O1-vac	Ce	0	9.60	4+
Oxygen-deficient slabs								
		O2	1.54		Ce2	0.97	9.85	3+
		O3	2.56		Ce3	0.97	9.86	3+
	$Ce_{0.963}Pr_{0.037}O_{2-x}$(1 1 1) with a surface O1-, O2- or O3-vacancy	O1	1.00	Surface O1-vac	Ce	0	9.60	4+
		O2	1.02		Ce4	0.96	9.92	3+
		O3	1.13		Pr	1.97	10.96	3+
	$Ce_{0.75}Pr_{0.25}O_{2-x}$(1 1 1) with a surface O1-, O2- or O3-vacancy	O1	1.00	Surface O1-vac	Ce	0	9.61	4+
		O2	0.50		Pr1	1.97	10.96	3+
		O3	0.83		Pr2	1.96*	10.89	3+

* spin down

(Ce4, Ce6) and (Ce5, Ce8) cation pairs, respectively (see Table 4). The removal of O2 and O3 from the 3.7 at% Pr-doped CeO_2(1 1 1) slab led to the reduction of the Pr cation as well as that of Ce2 or Ce7 atoms, respectively (see the location of Ce2 and Ce7 in Fig. 2). Nevertheless, the creation of O2- and O3-defect in the $Ce_{0.75}Pr_{0.25}O_2$(1 1 1) slab resulted in electron localization at Pr1 and Pr2 cations (see Table 4), similarly to what happened due to surface O1-defect creation. In this regard, we underline the 3.7 at% Pr-doped CeO_2(1 1 1) slab contains only one Pr cation, while that with 25 at% doping has four Pr ions. Therefore, the two electrons left by one oxygen removal could be localized on two Pr cations in the later slab.

In summary, the calculations indicated the electron density left behind by oxygen vacancy formation in Ce-Pr mixed oxides would preferentially be transferred to Pr cations. Besides, on the basis of the results shown in Tables 3 and 4, we emphasize the significant decrease of the energy needed for creating a single oxygen vacancy with the concomitant reduction of two tetravalent Pr cations. These findings indicate that oxygen donation and reducibility properties of ceria are enhanced by Pr dopant, and the main contribution to the reducibility of Pr-doped CeO_2 catalysts is due to Pr ions.

In a previous work [18], we have observed that addition of Pr to ceria samples notably increases the H_2 consumption in TPR experiments, particularly in the low-temperature reduction events (i.e. hydrogen consumption at T lower than 350 °C). In agreement with other works [86,87], this behavior has been associated with the reduction of Pr^{4+} to Pr^{3+} at the surface region. DFT calculations presented in the present work indicate that reduction of Pr^{4+} cations is favored with respect to that of Ce^{4+} cations, both for low and high Pr-doped CeO_2 materials, and also demonstrate that formation of oxygen vacancies associated with Pr^{4+}/Pr^{3+} redox couple requires less energy in comparison to Ce^{4+}/Ce^{3+} redox couple. Even more, from both theoretical calculations and experimental measurements performed in this work, we can conclude the OSC of Ce-Pr mixed oxides increases as the content of Pr added also increases.

Table 4
CeO_{2-x}(1 1 1) and Pr-doped CeO_{2-x}(1 1 1) systems. Reduced cations due to single O1-, O2- and O3-vacancy formation.

System	O-defect	Reduced cations
CeO_{2-x}(1 1 1)	O1	Ce2, Ce3
	O2	Ce4, Ce6
	O3	Ce5, Ce8
$Ce_{0.963}Pr_{0.037}O_{2-x}$(1 1 1)	O1	Pr, Ce4
	O2	Pr, Ce2
	O3	Pr, Ce7
$Ce_{0.75}Pr_{0.25}O_{2-x}$(1 1 1)	O1	Pr1, Pr2
	O2	Pr1, Pr2
	O3	Pr1, Pr2

The above mentioned ceria-based solids are considered as promising candidates for WGSR. Many authors have explained the good results obtained by proposing a redox reaction mechanism for catalysts supported over these reducible solids, which are active for oxygen transport and storage [88]. In such mechanism, ceria-based oxides become reduced due to CO oxidation and, then, these non-stoichiometric oxides are reoxidized by means of water [89]. Therefore, the activity of Ce-Pr mixed oxides for WGSR must be linked to their OSC. In fact, Cao et al. reported a correlation between OSC and the WGS activity for a Pr-doped CeO_2-based system (a ternary Ce-Pr-Zr oxide) [90].

Bearing in mind that the Pr content in the Ce-Pr mixed oxides strongly affects their surface area, the activity of the samples was evaluated in terms of the WGSR rate per surface unit. Table 2 shows that an increase of Pr content markedly improves the intrinsic reaction rate (i.e. per active site), which rises almost three folds in CePr50 sample with respect to pure ceria. As it was previously stated, the ratio between experimental and theoretical OSC follows nearly the same trend as this intrinsic WGSR activity. Although we highlight here the correlation between Pr content in the mixed oxides and their intrinsic activity toward the WGS reaction, the addition of Pr is detrimental to the surface area of the samples. As a result, there exists an optimal Pr content in order to maximize the WGSR rate per mass of catalyst, as it was observed in our previous work [18].

5. Conclusions

In the present work we have studied Ce-Pr mixed oxides by several experimental characterization techniques and DFT calculations, in order to deeply understand the influence of Pr addition. Sample precursors were synthesized by the urea method, with simultaneous precipitation of cerium and praseodymium cations for all the Pr contents analyzed. Thermal gravimetric analysis under oxygen atmosphere of the mixed precursors showed a promoting effect of Ce in the decomposition process of the samples with moderate Pr content. According to XRD results, Ce-Pr solid solutions with a slight increase of lattice parameter with Pr content were obtained after the calcination step at 450 °C. The growth of the lattice parameter would be due to a partial replacement of tetravalent ions by Ce^{3+} or Pr^{3+}. Raman spectra showed that Pr addition favors lattice defects and oxygen vacancies formation. Tetravalent ions replacement by trivalent ones is confirmed by XPS measurements. The take-off angle analysis indicated that Ce^{3+} ions are located mainly at the surface. Pr addition decreases Ce^{3+} concentration as determined by XPS suggesting that Pr preferentially replaces Ce surface ions. Addition of Pr increases the oxygen storage capacity per surface unit, which is in good agreement with the increase of oxygen vacancies observed by Raman measurements. On the other hand, first-principles calculations showed that the energy required to form a vacancy is lower for Pr-doped samples with respect to pure ceria. After oxygen removal, Pr cations are preferentially reduced even if there are Ce cations located closer to the vacancy than Pr one. Therefore XPS and Raman measurements, and DFT calculations allow us to conclude that the addition of Pr to ceria enhances the OSC of the Ce-Pr samples. WGSR rate per surface unit increases as Pr content increases following the same trend as OSC. In conclusion, the results obtained in this work indicate that the incorporation of an aliovalent cation like Pr and the simultaneous presence of Ce^{3+}/Ce^{4+} and Pr^{3+}/Pr^{4+} couples play a key role in developing high performance WGSR catalysts.

Acknowledgment

The authors acknowledge to the University of Buenos Aires (UBA), ANPCyT and CONICET for their financial support. Special thanks are given to ANPCyT for Grant PME 8-2003 to finance the purchase of the UHV Multi Analysis System.

Appendix A. Supplementary data

Supplementary data associated with this article can be found, in the online version, at http://dx.doi.org/10.1016/j.apcata.2014.07.040.

References

[1] D. Shchukin, R. Caruso, Chem. Mater. 16 (2004) 2287–2292.
[2] K. Schermanz Mining Production, Application and Safety Issues of Cerium-based Materials, in: A. Trovarelli (Ed.), Catalysis by Ceria and Related Materials, Imperial College Press, London, (2002), pp: 1–15.
[3] B. Smets, Mater. Chem. Phys. 16 (1987) 283–299.
[4] M. Funabiki, T. Yamada, K. Kayano, Catal. Today 10 (1991) 33–43.
[5] H. Li, G. Lu, Y. Wang, Y. Gou, Y. Gou, Cat. Comm. 11 (2010) 946–950.
[6] E. Su, C. Montreuil, W. Rothschild, App. Catal. 17 (1985) 75–86.
[7] G. Colón, F. Valdivieso, M. Pijolat, R. Baker, J. Calvino, S. Bernal, Catal. Today 50 (1999) 271–284.
[8] B. Yue, R. Zhou, Y. Wang, X. Zheng, Appl. Cat. A: Gen. 295 (2005) 31–39.
[9] B. Reddy, L. Katta, G. Thirmuthulu, Chem Mater. 22 (2010) 467–475.
[10] A. Hartridge, M. Ghanashyam Krishna, A. Bhattacharya, Mater. Sci. Eng. 57 (1999) 173–178.
[11] Y. Tang, H. Zhang, L. Cui, C. Ouyang, S. Shi, W. Tang, H. Li, J. Lee, L. Chen, Phys. Rev. B 82 (2010) 125104, 1-9.
[12] K. Ahn, D. Su Yoo, D. Hari Prasad, H.-W. Lee, Y.-Ch. Chung, J.-H. Lee, Chem. Mater. 24 (2012) 4261–4267.
[13] M. Luo, Z. Yan, L. Jin, J. Mol. Cat. A: Chem. 260 (2006) 157–162.
[14] Z. Pu, X. Liu, A. Jia, Y. Xie, J. Lu, M. Lou, J. Phys. Chem. C 112 (2008) 15045–15051.
[15] M. Malecka, L. Kepinski, W. Mista, Appl. Catal. B: Environ. 74 (2007) 290–298.
[16] Y. She, Q. Zheng, L. Li, Y. Zhan, C. Chen, Y. Zheng, X. Ling, Int. J. Hydr. Energy 34 (2009) 8929–8936.
[17] J. Lin, P. Biswas, V. Guliants, S. Misture, Appl. Catal. A: Gen. 387 (2010) 87–94.
[18] E. Poggio Fraccari, F. Mariño, M. Laborde, G. Baronetti, Appl. Catal. A: Gen. 460 (2013) 15–20.
[19] M. Jobbagy, F. Mariño, B. Schonbrod, G. Baronetti, M. Laborde, Chem. Mater. 18 (2006) 1945–1950.
[20] E. Poggio, M. Jobbágy, M. Moreno, M. Laborde, F. Mariño, G. Baronetti, Int. J. Hydr. Energy 36 (2001) 15899–15905.
[21] M. Romeo, K. Bak, J. El Fallah, F. Le Normand, L. Hilaire, Surf. Int. Sci. 20 (1993) 508–512.
[22] G. Kresse, J. Furthmuller, Comput. Mater. Sci. 6 (1996) 15–50.
[23] G. Kresse, J. Hafner, Phys. Rev. B 47 (1993) 558–561.
[24] G. Kresse, D. Joubert, Phys. Rev. B 59 (1999) 1758–1775.
[25] J. Perdew, K. Burke, M. Ernzerhof, Phys. Rev. Lett. 77 (1996) 3865–3868.
[26] H. Monkhorst, J. Pack, Phys. Rev. B 13 (1976) 5188–5192.
[27] S. Dudarev, G. Botton, S. Savrasov, C. Humphreys, A. Sutton, Phys. Rev. B 57 (1998) 1505–1509.
[28] V. Anisimov, J. Zaanen, O. Andersen, Phys. Rev. B 44 (1991) 943–954.
[29] M. Nolan, S. Grigoleit, D. Sayle, S. Parker, G. Watson, Surf. Sci. 576 (2005) 217–229.
[30] H. Li, H. Wang, X. Gong, Y. Guo, Y. Guo, G. Lu, P. Hu, Phys. Rev. B 79 (2009) 193401, 1-4.
[31] C. Castleton, J. Kullgren, K. Hermansson, J. Chem. Phys. 127 (2007) 244704, 1-11.
[32] M. Nolan, S. Grigoleit, D. Sayle, S. Parker, G. Watson, Surf. Sci. 576 (2005) 217.
[33] N.V. Skorodumova, M. Baudin, K. Hermansson, Phys. Rev. B: Condens. Matter Mater. Phys. 69 (2004) 075401.
[34] Z.X. Yang, T.K. Woo, M. Baudin, K. Hermansson, J. Chem. Phys. 120 (2004) 7741.
[35] D.M. Lyons, J.P. McGrath, M.A. Morris, J. Phys. Chem. B 107 (2003) 4607.
[36] G. Henkelman, A. Arnaldsson, H. Jónsson, Comput. Mater. Sci. 36 (2006) 354–360.
[37] M. Jobbagy, G. Soler Illia, A. Regazzoni, M. Blesa, Chem. Mater. 10 (1998) 1632–1637.
[38] G. Soler-Illia, R. Candal, A. Regazzoni, E. Blesa, Chem. Mater. 9 (1997) 184–191.
[39] F. Rorif, J. Fuger, J. Desreaux, Radiochim. Acta 93 (2005) 103–110.
[40] M. Jobbágy, C. Sorbello, E. Sileo, J. Phys. Chem. C 113 (2009) 10853–10857.
[41] S. Somacescu, V. Parvulescu, J. Calderon-Moreno, S. Suh, P. Osiceanu, B. Su, J. Nanopart. Res. 14 (2012) 885–1002.
[42] Y. Zhang, K. Han, X. Yin, Z. Fang, Z. Xu, W. Zhu, J. Cryst. Growth 311 (2009) 3883–3888.
[43] A. Tok, S. Du, F. Boey, W. Chong, Mater. Sci. Eng. A 466 (2007) 223–229.
[44] T. Rojas, M. Ocaña, Scr. Mater. 46 (2002) 655–660.
[45] B. Reddy, G. Thrimurthulu, L. Katta, J. Phys. Chem. C 113 (2009) 15882–15890.
[46] Z. Song, W. Liu, H. Nishiguchi, A. Takami, K. Nagaoka, Y. Takita, Appl. Catal. A: Gen. 329 (2007) 86–92.
[47] K. Ryan, J. McGrath, R. Farrel, W. O'Neill, C. Barnes, M. Morris, J. Phys.: Condens. Mater. 15 (2003) L49–L58.
[48] D. Kim, J. Am. Ceram. Soc. 72 (1989) 1415–1421.
[49] S. Tsunekawa, R. Sivamohan, S. Ito, A. Kasuya, T. Fukuda, Nano. Mater. 11 (1999) 141–147.
[50] S. Hong, A. Virkar, J. Am. Ceram. Soc. 78 (1995) 433–439.
[51] V. Glushkova, F. Hanic, L. Sazonova, Ceramurgia Int. 4 (1978) 176–178.
[52] T. Zhang, J. Li, H. Li, Y. Li, W. Shen, Catal. Today 148 (2009) 179–183.
[53] Z. Wu, M. Li, S. Overbury, J. Catal. 285 (2012) 61–73.
[54] H. Wang, C. Lu, Mater. Res. Bull. 37 (2002) 783–792.
[55] M. Zaki, G. Hussein, S. Mansour, H. Ismail, G. Mekhemmer, J. Colloids Surf. 127 (1997) 47–56.
[56] A. Bensalem, F. Bozon-Verduraz, M. Delamar, G. Bugli, Appl. Catal. A: Gen. (1995) 81–93.
[57] Z. Pu, J. Lu, M. Luo, Y. Xie, J. Phys. Chem. C 111 (2007) 18695–18702.
[58] J. Mc Bride, K. Hass, B. Poindexter, W. Weber, J. Appl. Phys. 76 (1994) 2435–2441.
[59] P. Fang, M. Luo, J. Lu, S. Cen, X. Yan, X. Wang, Thermochim. Acta 478 (2008) 50–54.
[60] I. Kosacki, T. Suzuki, H. Anderson, P. Colomban, Solid State Ionics 149 (2002) 99–105.
[61] J. Spanier, R. Robinson, F. Zhang, S. Chan, H. Herman, Phys. Rev. B 64 (2001) 245407–245515.
[62] L. Li, F. Chen, J. Lu, M. Luo, J. Phys. Chem. A 115 (2011) 7972–7977.
[63] P. Burroughs, A. Hamnett, A. Orchad, G. Thornton, J Chem. Soc. Dalton Trans. 17 (1976) 1686–1698.
[64] J. Shyu, W. Weber, H. Gandhi, J. Phys. Chem. 92 (1988) 4964–4970.
[65] T. Bart, C. Fries, F. Cariati, J. Bart, N. Giordano, J. Chem. Soc. Dalton Trans. 9 (1983) 1825–1829.
[66] R. Leppelt, B. Schumacher, V. Plzak, M. Kinne, R. Behm, J. Catal. 244 (2006) 137–152.
[67] F. Zhang, P. Wang, J. Koberstein, S. Khalid, S. Chan, Surf. Sci. 563 (2004) 74–82.
[68] A. Laachir, V. Perrichon, A. Badri, J. Lamotte, E. Catherine, J. Lavalley, J. Chem. Soc. Faraday Trans. 87 (1991) 1601–1609.
[69] S. Hofmann, Depth Profiling in AES and XPS, in: D. Briggs, M. Seah (Eds.), Practical Surface Analysis, John Wiley & Sons, New York, 1996, pp. 143–199.
[70] J. Thomas, S. Hofmann, J. Vac. Sci. Technol. A 185 (1984) 1921–1928.
[71] M. Seah, Quantification of AES and XPS, in: D. Briggs, M. Seah (Eds.), Practical Surface Analysis, John Wiley & Sons, New York, 1996, pp. 201–255.
[72] S. Hofmann, J. Sanz, Surf. Interf. Anal. 6 (1984) 75–77.

[73] V. Ivanov, A. Scherbakov, A. Usatenko, Russian Chem. Rev. 78 (2009) 855–871.
[74] L. Wu, H. Wiesmann, A. Moondenbaugh, R. Klie, Y. Zhu, D. Welch, M. Suenaga, Phys. Rev. B 69 (2004) 125415–125419.
[75] S. Rossignol, C. Descorme, C. Kappenstein, D. Duprez, J. Mater. Chem. 11 (2001) 2587–2592.
[76] C. Hori, H. Permana, K. Simon Ng, A. Brenner, K. More, K. Rahmoeller, D. Betton, Appl. Catal. B: Environ. 16 (1998) 105–117.
[77] Y. Madier, C. Descorme, A. Le Govic, D. Duprez, J. Phys. Chem. 103 (1999) 10999–11006.
[78] J. Paier, C. Penschke, J. Sauer, Chem. Rev. 113 (2013) 3949–3985.
[79] Y. Tang, H. Zhang, L. Cui, Ch. Ouyang, S. Shi, W. Tang, H. Li, J.-S. Lee, L. Chen, Phys. Rev. B 82 (2010) 125104.
[80] A. Bianconi, A. Kotani, K. Okada, R. Giorgi, A. Gargano, A. Marcelli, T. Miyahara, Phys. Rev. B 38 (1988) 3433.
[81] H. Ogasawara, A. Kotani, K. Okada, B.T. Thole, Phys. Rev. B 43 (1991) 854.
[82] S.M. Butorin, L.C. Duda, J.H. Guo, N. Wassdahl, J. Nordgren, M. Nakazawa, A. Kotani, J. Phys.: Condens. Matter. 9 (1997) 8155.
[83] A. Hartridge, M.G. Krishna, A.K. Bhattacharya, Mater. Sci. Eng. B 57 (1999) 173.
[84] N.V. Skorodumova, S.I. Simak, B.I. Lundqvist, I.A. Abrikosov, B. Johansson, Phys. Rev. Lett. 89 (2002) 166601.
[85] M. Ganduglia-Pirovano, J.L. Da Silva, J. Sauer, Phys. Rev. Lett. 102 (2009) 026101.
[86] R. Long, J. Luo, M. Chen, H. Wan, Appl. Catal. A: Gen. 159 (1997) 171–185.
[87] C. Lopez-Cartes, S. Bernal, J. Calvino, M. Cauqui, G. Blanco, J. Perez-Omil, J. Pintado, S. Helveg, P. Hansen, Chem. Commun. 5 (2003) 644–645.
[88] Y. Li, Q. Fu, M. Flytzani-Stephanopoulos, Appl. Catal. B: Environ. 27 (2000) 179–191.
[89] X. Qi, M. Flytzani-Stephanopoulos, Ind. Eng. Chem. Res. 43 (2004) 3055–3062.
[90] L. Cao, C. Ni, Z. Yuan, S. Wang, Cat. Comm. 10 (2009) 1192–1195.